Available online at www.sciencedirect.com
SCIENCE DIRECT®
Journal of Solid State Chemistry 177 (2004) 1098–1110
JOURNAL OF SOLID STATE CHEMISTRY
http://elsevier.com/locate/jssc

Phase transitions and electrical transport in the mixed-valence V^{2+}/V^{3+} oxide $BaV_{10}O_{15}$

C.A. Bridges and J.E. Greedan*

Department of Chemistry and Brockhouse Institute for Materials Research McMaster University, 1280 Main St. w., Hamilton, Ont., Canada L8S 4M1

Received 21 July 2003; received in revised form 8 October 2003; accepted 14 October 2003

Abstract

$BaV_{10}O_{15}$ can be regarded as a Ba-doped V_2O_3 in which the Ba^{2+} ions substitute in the O^{2-} close-packed layers. The Ba^{2+} ions order within these layers and direct the occupation of the octahedral sites by V^{2+} and V^{3+} ions resulting in a structure with subtle differences from that of V_2O_3 which can be described in *Cmca* at room temperature. Magnetic susceptibility data show evidence for two phase transitions at 135 and 40 K. The higher temperature transition at 135 K is shown to be structural in origin to another orthorhombic form, *Pbca*. The structural transition temperature, T_s, decreases with decreasing V^{2+} content to a minimum value of 105 K. Crystallographic and DSC data support a first-order transition driven by partial bond formation which results in a 7% reduction in the distance between two of the five crystallographically distinct V atoms. There is no conclusive crystallographic evidence for V^{2+}/V^{3+} charge ordering in either the *Cmca* or *Pbca* forms. Electrical conductivity data show semiconducting behavior above T_s which can be fitted to a small polaron hopping model for the most reduced samples ($T_s = 135$ K). The same sample shows a sharp but not discontinuous decrease in conductivity below T_s, consistent with carrier removal due to bond formation. More oxidized materials with $T_s = 105$ K show a more subtle anomaly. Evidence for correlated (Efros-Shklovskii) variable-range hopping at low temperatures is seen in the $T_s = 105$ K sample from analysis using a Hill-Zabrodski ($\log dE$ vs. $\log T$) plot. Thermopower data on the $T_s = 135$ K material show an anomalously small value of $S \sim +1\,\mu V/K$ at room temperature which increases to $> +200\,\mu V/K$ upon cooling to 90 K. Plots of dS/dT show evidence for the $T_s = 135$ K phase transition. These results are not consistent with a simple one carrier model for small polaron hopping assuming that the V^{2+} ions are the carriers, which would predict $S \sim -100\,\mu V/K$, but seem to demand a two carrier model with $n \sim p$ at room temperature for which n-type carriers are trapped as a result of bond formation at the phase transition as temperature is lowered. The lower temperature phase transition near 40 K is magnetic in origin and will be discussed in a subsequent publication.

Keywords: V^{2+}/V^{3+} mixed valence oxide; First order crystallographic phase transition; Partial V–V bond formation; Electrical conductivity; Magnetic susceptibility; Thermoelectric power; Electron trapping; Small polaron hopping; Variable range hopping

1. Introduction

Transition metal oxides which exhibit strong electronic correlation have attracted extraordinary attention over the past few decades. One material which has been central to experimental and theoretical studies of correlated systems is V_2O_3 for which a literature of more than 3000 publications exists. This material crystallizes in the well-known corundum structure, which consists of a hexagonal close-packed sublattice of oxide ions in which V^{3+} occupies $\frac{2}{3}$ of the octahedral sites. Surprisingly, given its apparent crystallographic simplicity, V_2O_3 exhibits a rich variety of properties including a spectacular metal/insulator transition below ~ 160 K associated with a first-order crystallographic phase transition from $R\bar{3}c$ to $I2/a$ [1,2]. The monoclinic form is insulating and antiferromagnetic [3] and is often regarded as a canonical Mott-Hubbard insulator [4–6], though recent results indicate a more complex picture [7]. The material shows a remarkable sensitivity to applied pressure and doping with small amounts of adjacent ions, especially Cr^{3+} [8,9].

As vanadium exhibits a wide range of stable oxidation states in oxides, from 2+ to 5+, a large number of mixed-valence vanadium oxides exist, many of which show phenomena of current interest. NaV_2O_5, a V^{4+}/V^{5+} material, shows both charge ordering and spin gap

*Corresponding author. Fax: +905-522-2773.
E-mail address: greedan@mcmail.cis.mcmaster.ca (J.E. Greedan).

0022-4596/$ - see front matter © 2003 Elsevier Inc. All rights reserved.
doi:10.1016/j.jssc.2003.10.025

formation at low temperatures [10]. The binary oxides, V_4O_7 and V_5O_9 show both metal/insulator transitions and charge (V^{3+}/V^{4+}) ordering [11,12].

Other vanadium oxides with related structures and chemistry are worthy of interest but have been less well studied. A number of materials with structures derived from magneto-plumbite have been reported with composition MV_6O_{11} ($M = Na, K, Sr, Pb$) and hollandite-based phases, $Ba_xV_8O_{16}$ and $BaV_{10-x}O_{17}$, for example, [13–18]. NaV_6O_{11} is the best studied member of this series and shows a range of interesting properties including crystallographic phase transitions and metallic weak ferromagnetism [19–21]. A partial form of magnetic frustration is also known, as one set of V sites (out of three) in the crystal structure forms a Kagome lattice [22]. All of the above materials involve mixed-valence V^{4+}/V^{3+}, both of which are common oxidation states for vanadium oxides.

Considerably less is known about mixed valence vanadium oxides involving the rare +2 oxidation state. To our knowledge only three such ternary oxides are known, each with the V^{2+}/V^{3+} combination: the spinel AlV_2O_4 with average oxidation state +2.5 [23], $MV_{13}O_{18}$ with average oxidation state +2.62 [24,25], and $MV_{10}O_{15}$ [26,27] with average oxidation state +2.80, where M = Ba or Sr. The crystal structures of the latter two can be described in terms of close-packed layers of Ba^{2+} and O^{2-} with vanadium ions occupying octahedral sites, with different symmetries, $R\bar{3}$ for $MV_{13}O_{18}$ and *Cmca* for $MV_{10}O_{15}$. The study of the physical properties of these materials is in the very early stages. AlV_2O_4 shows a structural phase transition from *Fd3m* to $R\bar{3}m$ below 700 K and accompanying small anomalies in both resistivity and susceptibility. The phase transition is ascribed to a very weak charge ordering described as $V^{+2.5-\delta}/V^{+2.5+3\delta}$, where $\delta \sim 0.1$ [23]. Both $BaV_{13}O_{18}$ and $SrV_{13}O_{18}$ are described as n-type semiconductors but the resistivity values are in the mΩ cm range and the Seebeck coefficients range from −10 to −50 μV/K. The magnetic susceptibilities are significantly smaller than expected based on a local moment model for the V ions. A coherent understanding of the properties of these materials is not yet available.

Turning to the other series, $MV_{10}O_{15}$, more specifically $BaV_{10}O_{15}$, which is the subject of this report, a more detailed description of its crystal structure and the close relationship to that of V_2O_3 is in order. $BaV_{10}O_{15}$ can be considered to result from "doping" of V_2O_3 with Ba^{2+}. One obvious result of such doping is the reduction of 20% of the V^{3+} ions to V^{2+}, a rare oxidation state for this element in oxides as already mentioned. As well, due to the negligible difference in effective radii, 1.42 Å for both Ba^{2+} and O^{2-} in VIII-fold coordination [28], the barium ions substitute in the closed-packed oxide sublattice. Due to electrostatic forces, the Ba^{2+} ions order within a close-packed layer occupying $\frac{1}{8}$ of the sites in layers of composition BaO_7 which alternate with O_8 layers [27]. The stacking of the layers is modified from strict *hcp* as in V_2O_3 to alternating *hcp* and cubic close-packing, *ccp*, Fig. 1a.

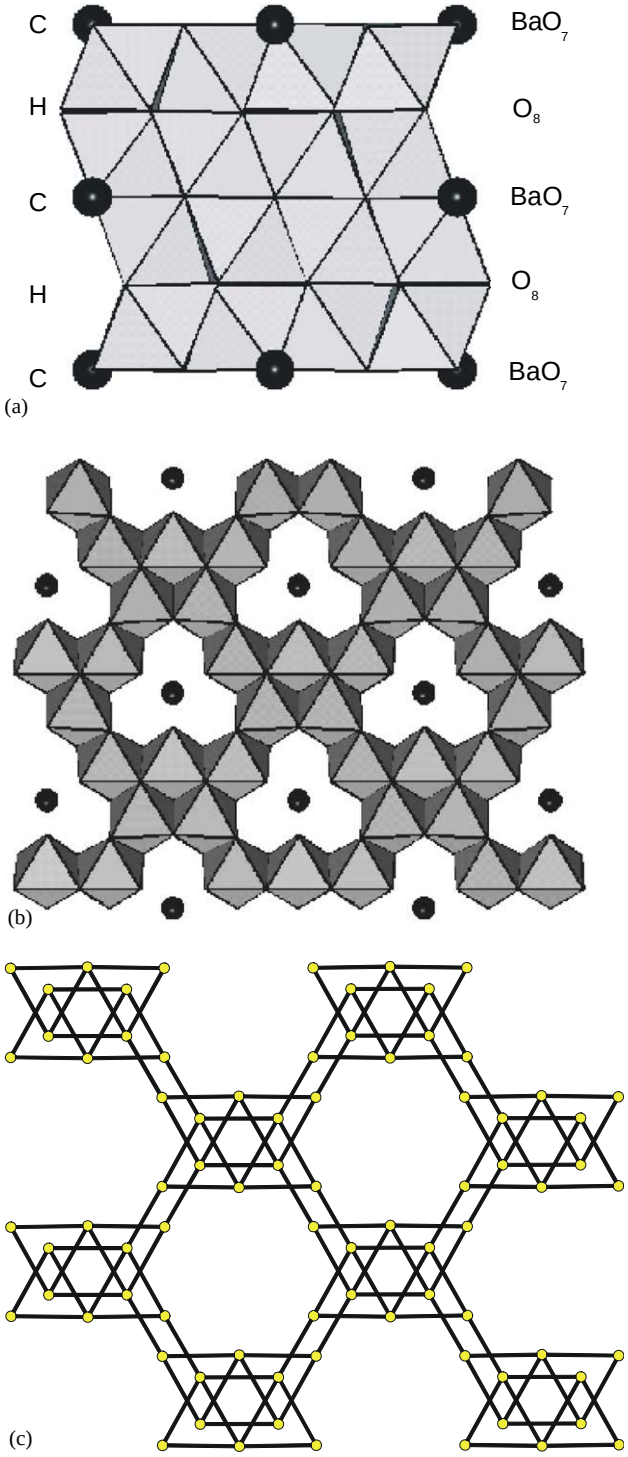

Fig. 1. (a) Stacking of the BaO_7 and O_8 close-packed layers normal to the *c*-axis in an alternating *hcp* and *ccp* sequence. (b) Occupation of the V octahedral sites within a close-packed layer. (c) The V sublattice in two layers showing the presence of V_{10} clusters and the condition for geometric magnetic frustration, i.e., edge sharing tetrahedra.

Electrostatic repulsion, due the presence of Ba^{2+} in the close-packed layers, directs the occupation of the octahedral sites by the V^{3+} and V^{2+} ions, as shown in Fig. 1b. The possibility of charge ordering on the octahedral sites arises due the occurrence two-oxidation states of vanadium, an issue which will be addressed in the following section. As mentioned, a very slight degree of charge ordering has been claimed for the spinel AlV_2O_4 [23]. The other remarkable feature of this structure type is the topology of the *M* sublattice shown in Fig. 1c, which is seen to consist of interconnected M_{10} clusters of edge-shared tetrahedra and thus provides a necessary condition for geometric magnetic frustration. Evidence for frustrated magnetism has been demonstrated for $BaCr_{10}O_{15}$ [27]. Thus, $BaV_{10}O_{15}$ represents a material with the potential for highly correlated electronic behavior, charge ordering and geometric magnetic frustration. In this work a remarkable structural phase transition will be investigated by means of a detailed crystallographic study, electrical conductivity and thermopower measurements. Subsequent papers will describe the effects of chemical substitutions and unusual magnetic properties associated with the geometric frustration.

2. Experimental

2.1. Synthesis

Previous reports from this laboratory indicated that both $SrV_{10}O_{15}$ and $BaV_{10}O_{15}$ could be prepared using the reaction Scheme (I) below at 1350°C for 24 h [27]:

$$BaCO_3 + 5V_2O_3 + H_2 \rightarrow BaV_{10}O_{15} + H_2O + CO_2 \quad (I)$$

Recent attempts using this approach resulted in substantially pure samples but in all cases varying amounts of VO_x were always present. Refiring under the same conditions led to the diminution of the amount of $BaV_{10}O_{15}$ in the product, raising the possibility that this compound is metastable at 1350°C. This led to another approach, Scheme (II) below, using much higher temperatures, 1550–1600°C for 17 h in inert (Ar) gas atmosphere:

$$Ba_3V_2O_8 + 10VO + 9V_2O_3 \rightarrow 3BaV_{10}O_{15} \quad (II)$$

$Ba_3V_2O_8$ was prepared in air at 950°C by reacting $BaCO_3$ and V_2O_5 for 24 h. Hydrogen reduction of V_2O_5 at 700°C for 24 h yielded V_2O_3, the oxygen content of which was monitored by thermal gravimetric analysis (TGA). VO was synthesized by arc melting V metal and V_2O_3, and with TGA analysis of the oxygen content. The starting materials in (2) were sealed in a molybdenum crucible by welding under an atmosphere of ultrapure argon gas. Radio-frequency induction heating was used to attain the indicated temperatures, which were measured using an optical pyrometer. For most of the runs the sample was heated to the reaction temperature over 7 h, held for 17 h and quenched by turning off the RF generator. This approach generally resulted in small grained polycrystalline samples. To encourage the growth of crystals a variant was used in which the crucible was cooled over 6 h from the reaction temperature to 1400°C, followed by quenching. This approach resulted in crystals of dimension 0.1–0.5 mm which were suitable for single crystal X-ray diffraction.

2.2. Chemical analysis

The samples were analyzed by gravimetric oxidation using a Netzsch STA409 to measure the weight gain in air. As well, the Ba:V ratio was measured by Inductively Coupled Plasma Mass Spectrometry (ICPMS) on a Perkin-Elmer Elan 6100. The samples were dissolved in aqua regia at room temperature overnight, and diluted by a factor of 10^5. A calibration curve, created from standard barium and vanadium solutions, was used to determine the concentrations of these species for the analysis.

2.3. X-ray powder diffraction

A Guinier-Hågg camera (Cu$K\alpha_1$ $\lambda = 1.54056$ Å) was used to monitor phase purity and determine unit cell constants. For the latter purpose an internal standard of high purity Si powder was added.

2.4. X-ray single crystal diffraction

Data were obtained on a Siemens/Bruker P4 four-circle diffractometer using a rotating anode Mo source and a 1 K CCD area detector (Bruker). SMART and SAINT software packages were used for data collection and processing, respectively [29]. The crystal was ground into a roughly spherical shape of dimension ~0.05 mm. Absorption and $\lambda/2$ corrections were performed using SADABS [30]. SHELXL97 was utilized for structure solution [31]. In some experiments the crystal was cooled and the temperature was controlled by an Oxford Cryostream Cooler. The sample temperature was monitored by a thermocouple placed ~2 mm from the crystal.

2.5. Powder neutron diffraction

Data were collected at the C2 diffractometer operated by the Neutron Program for Materials Research of the National Research Council of Canada, Chalk River, Canada, at wavelengths, $\lambda = 1.329$ and 2.379 Å. Samples were contained in closed cycle refrigerator with temperature control of ± 0.1 K.

2.6. DC magnetic susceptibility

A Quantum Design MPMS S.Q.U.I.D. magnetometer was utilized to collect susceptibility data over the temperature range 2–350 K at various applied fields. Data were taken in both the field-cooled (FC) and zero-field-cooled (ZFC) modes.

2.7. Electrical resistivity measurements

DC resistivity measurements were performed on dense, well sintered samples cut into the shape of elongated bars. A standard four-probe geometry was used and contacts were made using silver epoxy to silver wire potential and current leads. Either a Quantum Design PPMS or an Oxford Maglab measurement system was used. As the resistivity of the samples changed by more than 5 orders of magnitude over the temperature range investigated, currents between 0.01 and 100 μA were employed in various temperature regimes to give ohmic behavior and acceptable signal to noise. In all cases the average potential for both forward and reverse bias was used to compute the resistivity.

2.8. Thermoelectric power

Measurements of the Seebeck coefficient were measured using an apparatus constructed locally and described elsewhere [32]. Again, samples were in the form of bars cut from dense, well-sintered discs and contacts were made to the measuring heads using silver paste. Data could be collected, normally, over the range 35–350 K using a closed-cycle refrigerator.

2.9. Thermal analysis

Differential scanning calorimetry studies were carried out using a TA Instruments DSC 2910. Samples of 10–30 mg mass were sealed in thin aluminum discs for measurement. An empty aluminum disc was used as the reference. Temperatures are measured with Chromel and Alumel thermocouple wires attached directly under the sample and reference pans. The system was calibrated using indium. Sample cooling was attained using a liquid nitrogen cooling accessory within the range 110–155 K.

3. Results and discussion

3.1. Magnetic susceptibility

In previous work the magnetic susceptibility was not reported for $BaV_{10}O_{15}$ due to problems of small impurities and non-reproducibility of the results [27]. During the course of this study several samples of nominal composition $BaV_{10}O_{15}$ were prepared and characterized. Fig. 2a shows the inverse susceptibility behavior for a typical sample over the temperature range 2–350 K. There are several obvious features. First, note that the Curie–Weiss law appears to hold for $T > 140$ K. Fitting this regime yields the constants $C = 11.6(1)$ emu-K/mol and $\theta_c = -1156(15)$ K. The Curie constant can be compared with the spin-only value $2C(V^{2+} = 1.87) + 8C(V^{3+} = 1.00) = 11.74$ emu-K/mol, giving good evidence for the presence of the rare V^{2+}. The very large, negative Weiss temperature indicates strong antiferromagnetic spin correlations which is significant in view of the frustrated topology of the V sublattice. There is also evidence for complex behavior for $T < 135$ K, as at least three features can be seen: a continuous increase in the susceptibility (decrease in the inverse susceptibility) just below 135 K without a FC–ZFC divergence, an abrupt FC–ZFC

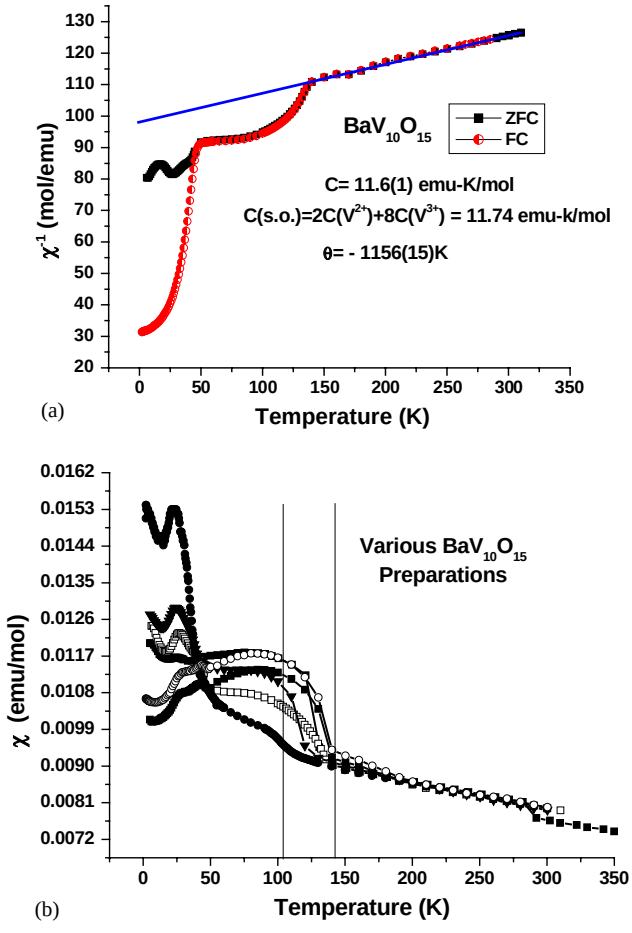

Fig. 2. (a) (TOP) Inverse magnetic susceptibility for $BaV_{10}O_{15}$ showing evidence for two-phase transitions below ~135 and ~40 K and a Curie–Weiss fit with the parameters shown. (b) (BOTTOM) Susceptibilities of several samples of nominal composition, $BaV_{10}O_{15}$ showing the variation of the high temperature phase transition, T_s, between the limits of 105 K (oxidized samples) to 135 K (nearly stoichiometric samples).

divergence below 50 K and a weak maximum at ~25 K in the ZFC data. Fig. 2b shows similar data, ZFC mode only, for several samples of varying composition. It is clear that all of the transitions are fairly robust with the onset for the highest temperature feature falling within an envelope between 105 and 135 K. It is the high temperature transition which will be the subject of this paper. Analytical data in the form of oxidative weight gain (theoretical = 19.85%) show a value of 19.7% for the samples with a transition at 135 K and 18.2% for that at 105 K, indicating that the decrease in transition temperature is apparently correlated with a decrease in V^{2+} content (decrease in weight gain). ICPMS data give a Ba:V ratio of 0.0978(4) for the sample with $T_s = 135$ K and 0.0973(4) for the $T_s = 105$ K material, i.e., evidence for a small Ba deficiency which does not vary significantly as a function of T_s.

3.2. Differential scanning calorimetry (DSC)

The thermodynamics of the high temperature transition was investigated using DSC as seen in Fig. 3 on a sample with a transition near 135 K. Clearly, first-order behavior is seen in the form of a latent heat and thermal hysteresis. The transition onset, T_s, was measured at 133.3 K upon heating and 130.6 K with cooling. The transition enthalpy was estimated by integrating the peak area. Two samples with $T_s = 133.9$ and 133.3 K gave $\Delta H_{TRANS} = 791$ and 978 J/mol, respectively. The associated entropy, $\Delta S_{TRANS} = \Delta H_{TRANS}/T_s$, is 5.9 and 7.3 J/mol-K for the two samples with an average of 6.6 J/mol-K. This value is comparable to the expected value for a two configuration problem, $\Delta S_{TRANS} = R \ln 2 = 5.6$ J/mol-K. The above observations suggest, strongly, a first-order crystallographic phase transition near 135 K in $BaV_{10}O_{15}$.

3.3. Crystal structure near the high temperature transition

3.3.1. Powder neutron diffraction

Powder neutron diffraction data were obtained for a sample showing a $T_s \sim 125$ K at several temperatures near the phase transition in the heating mode. Figs. 4 and 5 show the thermal evolution of a selected part of the diffraction pattern, indicating a sharp phase transition. Fig. 5 displays the thermal evolution of the refined unit cell constants. Note that all three cell constants change sharply at the transition with **a** and **c** increasing with decreasing temperature while **b** decreases. The magnitudes, [$\Delta\mathbf{a} = +0.026(2)$ Å, $\Delta\mathbf{c} = +0.033(2)$ Å, $\Delta\mathbf{b} = -0.052(2)$ Å], are such that the total volume change is very small. The transition temperature was estimated by locating minima in plots of the temperature derivative for each cell constant and the mean value for this sample is $T_s = 124.2(3)$ K.

3.3.2. Single crystal X-ray diffraction

Full data sets were collected at 130 and 100 K on a single crystal isolated from a preparation which showed a bulk $T_s \sim 125$ K. The reported temperature is that measured at a thermocouple about 2 mm from the sample. The 130 K data were consistent with the *Cmca* space group found at room temperature in the previous study [27]. The details are shown in Table 1a–d. The three occupied V sites, V1, V2 and V3, have multiplicities in the ratios 8:16:16, respectively, which does permit the possibility of V^{2+}/V^{3+} charge ordering. The expected V–O distances (sum of the Shannon radii) for a charge ordered material are V^{2+}–O = 2.15 Å and V^{3+}–O = 2.00 Å [28]. The weighted, average V–O distance is 2.03 Å and the corresponding Bond Valence Sum (BVS)

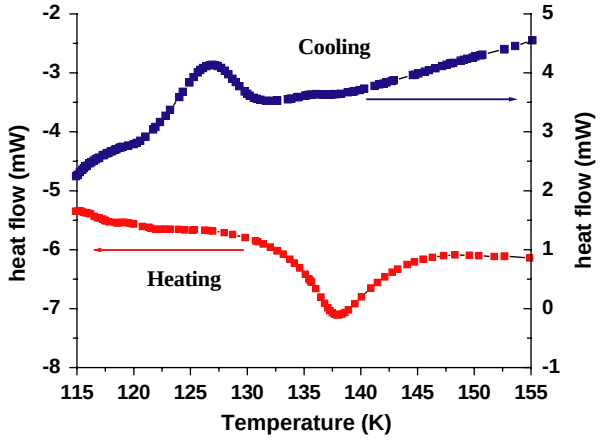

Fig. 3. Differential scanning calorimeter data for a sample of $BaV_{10}O_{15}$ in the range of the structural phase transition.

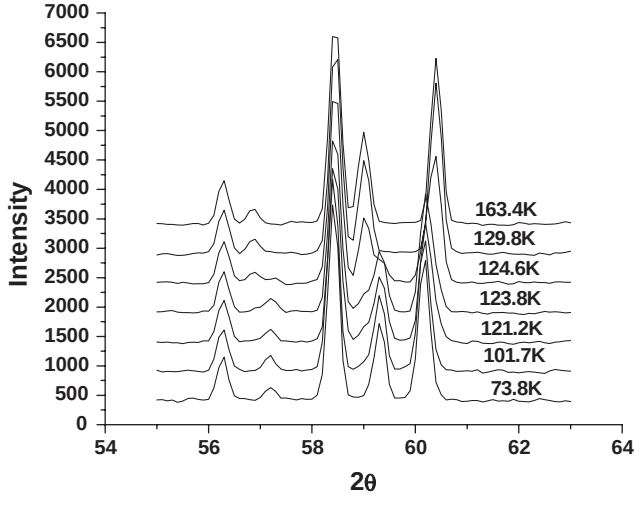

Fig. 4. Temperature evolution of a portion of the neutron diffraction pattern for a sample of $BaV_{10}O_{15}$ with $T_s \sim 125$ K.

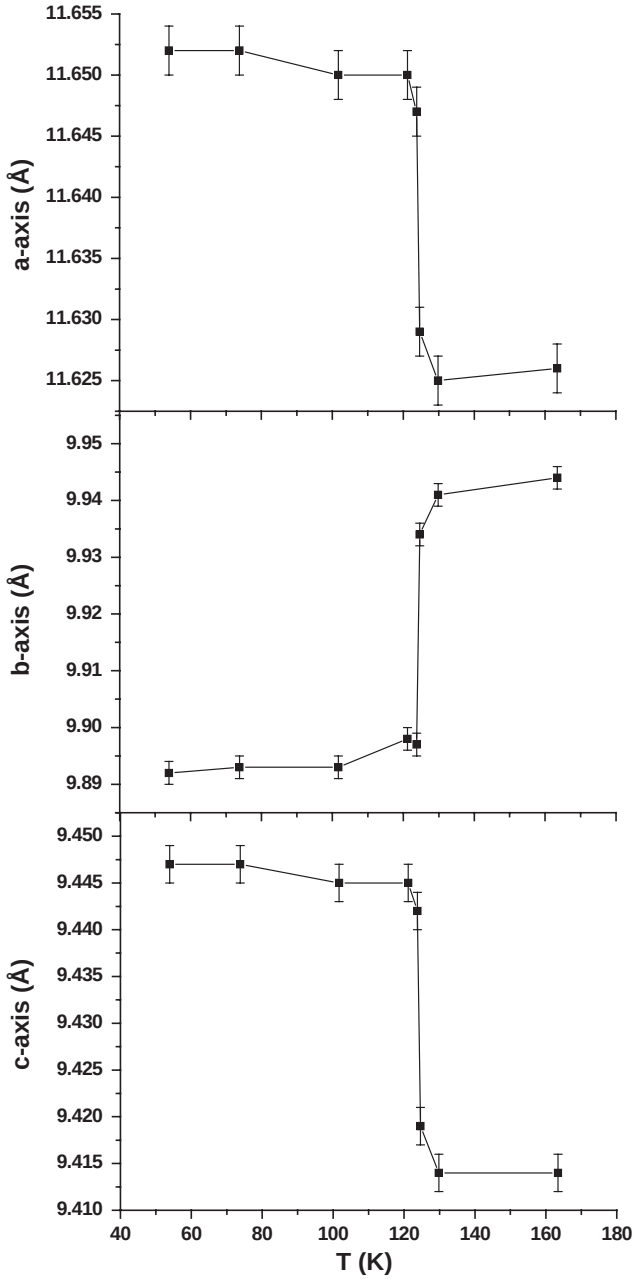

Fig. 5. Temperature dependence of the unit cell constants for the sample of Fig. 4. The transition temperature is estimated to be $T_s = 124.2(3)$ K. See text.

is 2.8 using the program VaList [33,34]. Examination of Table 1c and d indicates a random occupation of the V sites as had been observed at room temperature in the previous study [27].

The 100 K data showed a large number of weak reflections of the type $h + k + l = 2n + 1$ which violate the C-centering condition. The pattern of systematic absences was consistent with space group *Pbca*, a maximal, isomorphic subgroup of *Cmca*. Note that the mirror plane normal to **a** is also lost. A solution in *Pbca* for the 100 K data yielded agreement indices equivalent to those for *Cmca* at 130 K, Table 2a. As a result of the lowered symmetry, two of the V sites, V2 and V3, each split into eight-fold sites, denoted V2 and V2B and V3 and V3B in Table 2b. This splitting arises due to the aforementioned loss of the mirror plane. Given the apparent correlation of the onset temperature, T_s, with the V^{2+} content, it is reasonable to ask if charge ordering plays any role in the phase transition. Examination of Table 2c and d shows immediately that the verdict is negative, the average V–O distances and the BVS values remain nearly unchanged.

What, then, is the origin of the transition? The contents of Table 1c and 2c, aided by Fig. 6, indicate the changes in interatomic distances which result from the phase transition. A careful comparison of the V–V distances shows the following remarkable feature. Before the phase transition the V2–V3 distances alternate along a zig–zag path between 2.73 and 2.99 Å, the shorter separation links the V_{10} clusters and the longer corresponds to an edge of the cluster. At 100 K one intercluster distance (V3–V2B) shrinks markedly to 2.53 Å (from 2.73 Å) while the intracluster (V3–V2B) distance expands to 3.09 Å (from 2.99 Å). The former is one of the shortest V–V separations known in vanadium oxide chemistry. The relative V–V bond shrinkage involved, 7.3%, is also remarkable and comparable in magnitude to that seen in the well-known case of the phase transition in VO_2 in which V–V bond formation occurs, for which the reduction is 7.7% [35,36]. This may be taken as evidence for V–V bond formation, or at least bond strengthening, for this fraction of the V–V bonds in $BaV_{10}O_{15}$. The increase in intracluster V3–V2B bond length is only by 3.3%. Note that the other pair of inter- and intracluster V–V bonds, V2 and V3B, show the opposite trend but much less dramatically. The intercluster bond lengthens slightly (by 2.5%) to 2.80 Å and the intracluster bond decreases slightly (by 1.0%) to 2.96 Å. The overall enthalpy change is relatively small, ~0.8–1.0 kJ/mol, in comparison with VO_2, 4.69 kJ/mol [37]. This is not unreasonable given that only a fraction of the V–V bonds in $BaV_{10}O_{15}$ are involved in the shrinkage and that other V—V bond distances actually increase as a result of the phase transition. It is worth noting that the crystallographic phase transition in $BaV_{10}O_{15}$, in spite of the similarity in crystal structure, has little in common with that in V_2O_3, wherein the V–V distances increase as the symmetry is lowered from rhombohedral to monoclinic [2].

Further details of the crystal structure experiment can be obtained from the Fachinformationzentrum Karlsruhe, 76344 Eggenstein-Leopoldhafen, Germany (FAX: (49) 7247-808-666; email: crysdata@fiz-karlsruhe.de) on quoting the depository numbers (CSD) 413301 for $BaV_{10}O_{15}$ at 100 K and 413302 for $BaV_{10}O_{15}$ at 130 K.

Table 1

(a) $BaV_{10}O_{15}$ Details for the single crystal X-ray diffraction experiment at 130 K

Space group	*Cmca*	Refinement	
a (Å)	11.6015(9)	R1 ($I>2\sigma(I)$)	0.0214
b (Å)	9.9186(7)	wR2 ($I>2\sigma(I)$)	0.0528
c (Å)	9.3940(7)	R1 (all)	0.0229
V (Å^3)	1081.0(1)	wR2 (all)	0.0534
Temperature (K)	130	Goodness of fit	1.244
Radiation type	Mo $K\alpha$		
Color	Black	No. of reflections	1340
Index ranges	$-19\leqslant h\leqslant 18$	No. of parameters	68
	$-16\leqslant k\leqslant 11$	Extinction	0.0054(2)
	$-15\leqslant l\leqslant 12$	Mean shift/su	0.000

(b) Final atomic and isotropic displacement parameters in *Cmca* at 130 K. $T=\exp(h^2a*^2\,U^{11}+\cdots+2hka*b*\,U^{12}+\cdots)$

Site	*x*	*y*	*z*	U_i/U_e(Å^2)
Ba1	0	0.5	0	0.00468(7)
V1	0.5	0.67623(4)	0.13922(4)	0.00320(9)
V2	0.37097(3)	0.40976(3)	0.13548(3)	0.00667(8)
V3	−0.24606(3)	0.67201(3)	0.10991(3)	0.00464(7)
O1	−0.2541(2)	0.5	0	0.0066(3)
O2	0.1185(1)	0.2472(2)	0.0022(1)	0.0063(2)
O3	0.25	0.3257(2)	0.25	0.0046(3)
O4	0.6298(1)	0.5887(1)	0.2446(1)	0.0041(2)
O5	0.5	0.3429(2)	0.2477(2)	0.0045(3)
O6	0.5	0.5	0	0.0054(4)

(c) Selected bond distances (Å) for $BaV_{10}O_{15}$ in *Cmca* at 130 K

	Bond length		Bond length		Bond length
Ba–O5 (× 2)	2.836(2)	V1–O5	1.965(2)	V3–V3 [(a)]	2.5819(6)
Ba–O2 (× 4)	2.860(2)	V1–O4 (× 2)	2.000(1)	V3–V3 [(b)]	2.6336(6)
Ba–O1 (× 2)	2.949(2)	V1–O2 (× 2)	2.010(2)	V2–V3 [(c)]	**2.7317(5)**
Ba–O4 (× 4)	2.966(1)	V1–O6	2.183(1)	V2–V3 [(d)]	**2.8410(5)**
Mean	**2.903**	Mean	**2.028**	V1–V3 [(e)]	2.9592(4)
				V2–V3 [(f)]	**2.9872(5)**
V2–O5	1.947(1)	V3–O2	1.986(2)	V2–V2 [(g)]	2.9939(7)
V2–O3	1.9551(9)	V3–O1	1.9964(3)	V1–V2 [(h)]	3.0377(5)
V2–O2	2.028(2)	V3–O2	2.012(2)	V1–V2 [(i)]	3.1028(5)
V2–O4	2.049(1)	V3–O3	2.014(2)		
V2–O1	2.063(2)	V3–O4	2.088(1)		
V2–O6	2.1591(3)	V3–O4	2.091(1)		
Mean	**2.034**	Mean	**2.031**		

(d) Selected bond valence sums for $BaV_{10}O_{15}$ in *Cmca* at 130 K (in v.u.)

Atom	Bond valence*	Atom	Bond valence
Ba	2.266	O1	1.975
V1	2.760	O2	2.130
V2	2.724	O3	2.043
V3	2.710	O4	1.841
	Mean bond valence	O5	1.888
	V = 2.726	O6	1.866
	O = 1.971		

Note. Superscripts (a)–(i) on the V–V distances allow comparison with corresponding distances in the low temperature, *Pbca* phase (Table 2c). Entries in **bold** font show the largest changes resulting from the phase transition.

3.4. Electrical transport: conductivity

If V–V bond formation, involving at least some of the bonds in $BaV_{10}O_{15}$, is indeed the driving force for the crystallographic phase transition, one would expect consequences for the transport properties. Fig. 7 shows a simple Arrhenius plot of the temperature dependence of the conductivity for samples with T_s = 135 and 105 K. First, both samples are clearly semiconducting or insulating within the temperature interval

Table 2

(a) $BaV_{10}O_{15}$ details of the single crystal X-ray diffraction experiment at 100 K

Space group	*Pbca*	Refinement	
a (Å)	11.6155(9)	R1 ($I>2\sigma(I)$)	0.0227
b (Å)	9.8735(7)	wR2 ($I>2\sigma(I)$)	0.0536
c (Å)	9.4178(7)	R1 (all)	0.0278
V (Å^3)	1080.1(1)	wR2 (all)	0.0600
Temperature (K)	100	Goodness of fit	1.200
Radiation type	Mo $K\alpha$		
Colour	Black	No. of reflections	2556
Index ranges	$-18\leqslant h\leqslant 19$	No. of parameters	122
	$-16\leqslant k\leqslant 11$	Extinction	0.0029(1)
	$-12\leqslant l\leqslant 15$	Mean shift/su	0.000

(b) Final atomic and displacement parameters in *pbca* at 100 K. $T=\exp(h^2a*^2\,U^{11}+\cdots+2hka*b*\,U^{12}+\cdots)$

Site	*x*	*y*	*z*	U_i/U_e (Å^2)
Ba	0	0.5	0	0.00323(5)
V1	0.50407(3)	0.67522(4)	0.14202(4)	0.00201(7)
V2	0.37552(3)	0.41157(3)	0.13676(3)	0.00246(7)
V3	−0.24143(3)	0.67945(3)	0.11246(3)	0.00226(7)
V2B	0.63553(3)	0.09703(4)	0.63208(3)	0.00274(7)
V3B	0.24878(3)	0.82959(3)	0.60593(3)	0.00219(7)
O1	−0.2566(2)	0.5039(2)	0.0023(1)	0.0038(3)
O2	0.1141(1)	0.2505(2)	0.0064(2)	0.0036(2)
O2B	0.8793(1)	0.2545(2)	0.5040(2)	0.0033(2)
O3	0.2512(1)	0.3279(2)	0.2481(1)	0.0033(2)
O4	0.6332(1)	0.5884(2)	0.2451(2)	0.0032(2)
O4B	0.3725(1)	0.9116(2)	0.7444(2)	0.0031(2)
O5	0.5017(1)	0.3426(2)	0.2438(2)	0.0033(2)
O6	0.5	0.5	0	0.0038(4)

(c) Selected bond distances (Å) for $BaV_{10}O_{15}$ in *Pbca* at 100 K

	Bond length		Bond length		Bond length
Ba–O2 (× 2)	2.798(2)	V1–O5	1.973(2)	V3B–V3 [a]	2.5378(5)
Ba–O5 (× 2)	2.870(2)	V1–O4	1.981(2)	V3B–V3 [b]	2.6561(5)
Ba–O2B (× 2)	2.877(2)	V1–O4B	2.000(2)	**V3B–V2 [c]**	**2.7997(5)**
Ba–O4B (× 2)	2.958(2)	V1–O2B	2.002(2)	**V3–V2B [c]**	**2.5334(5)**
Ba–O1 (× 2)	2.981(2)	V1–O2	2.016(2)	**V3B–V2B [d]**	**2.7120(5)**
Ba–O4 (× 2)	2.986(2)	V1–O6	2.1873(4)	**V3–V2 [d]**	**2.9567(5)**
Mean	**2.912**	Mean	**2.027**	V3–V1 [e]	2.9696(5)
				V3B–V1 [e]	2.9851(5)
V2–O5	1.905(2)	V3–O3	1.971(2)	**V3B–V2 [f]**	**2.9636(5)**
V2–O3	1.967(2)	V3–O2	1.980(2)	**V3–V2B [f]**	**3.0869(5)**
V2–O4B	2.019(2)	V3–O2B	2.009(2)	V2B–V2 [g]	3.0217(6)
V2–O2B	2.041(2)	V3–O1	2.028(2)	V1–V2 [h]	3.0014(5)
V2–O1	2.078(2)	V3–O4B	2.092(2)	V2B–V1 [h]	3.0929(5)
V2–O6	2.1241(4)	V3–O4	2.119(2)	V2–V1 [i]	3.0958(5)
Mean	**2.022**	Mean	**2.033**		
V2B–O3	1.905(2)	V3B–O2B	1.994(2)		
V2B–O5	1.969(2)	V3B–O1	2.002(2)		
V2B–O1	2.014(2)	V3B–O2	2.010(2)		
V2B–O2	2.015(2)	V3B–O3	2.052(2)		
V2B–O4	2.118(2)	V3B–O4B	2.103(2)		
V2B–O6	2.2233(4)	V3B–O4	2.104(2)		
Mean	**2.041**	Mean	**2.044**		

(d) Selected bond valence sums for $BaV_{10}O_{15}$ in *Pbca* at 100 K (in v.u.)

Atom	Bond valence	Atom	Bond valence
Ba	2.245	O1	1.956
V1	2.774	O2	2.164
V2	2.812	O2B	2.119
V3	2.708	O3	1.741
V2B	2.724	O4	1.893
V3B	2.621	O4B	1.821
	Mean bond valence	O5	2.099
	$V=$ **2.728**	O6	1.864
	$O=1.966$		

Note. Superscripts (a)–(i) on the V–V distances allow comparison with corresponding distances in the high temperature, *Cmca* phase (Table 1c). Entries in **bold** font show the largest changes resulting from the phase transition.

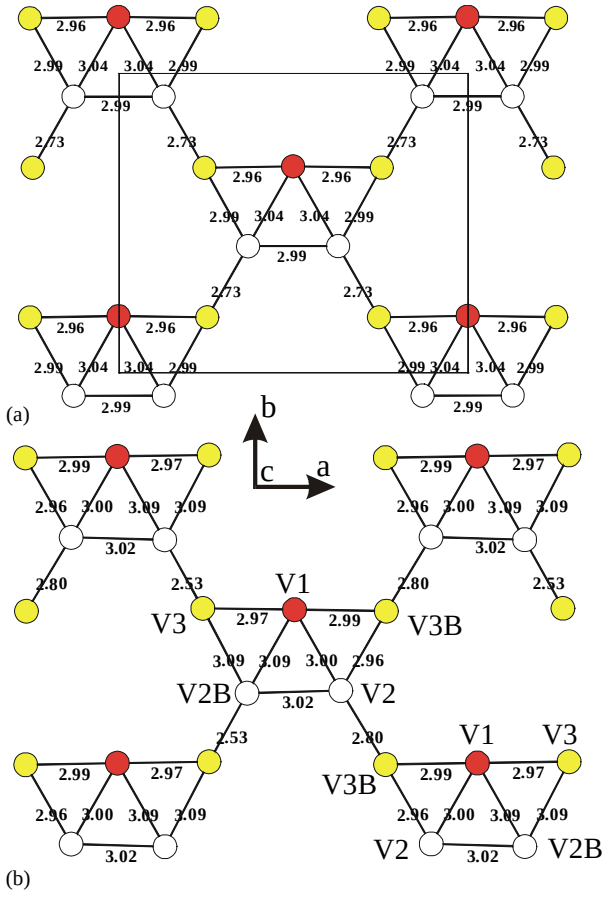

Fig. 6. Comparison of V–V distances in one V layer between the high temperature form, *Cmca* (a, top), and the low temperature form, *Pbca* (b, bottom). See text for discussion and Tables 1c and 2c.

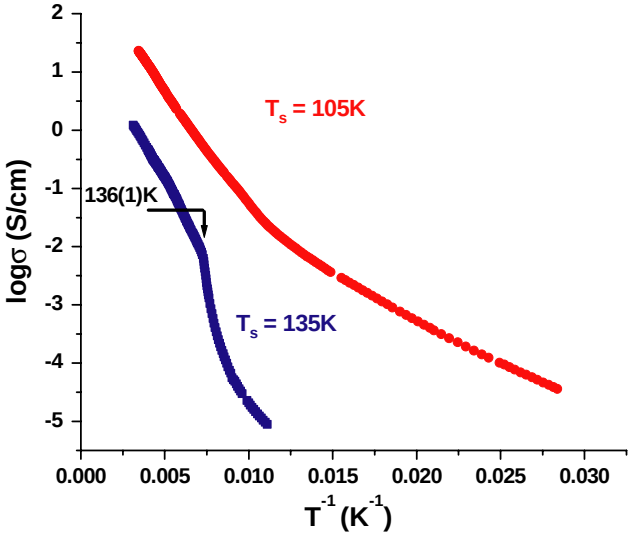

Fig. 7. Temperature dependence of the conductivity of $BaV_{10}O_{15}$ samples with $T_s = 105$ and 135 K.

studied, ~30–300 K, and the conductivity varies over a range of $\sim 10^5$. The conductivity of the $T_s = 105$ K sample is always greater than that of the $T_s = 135$ K sample.

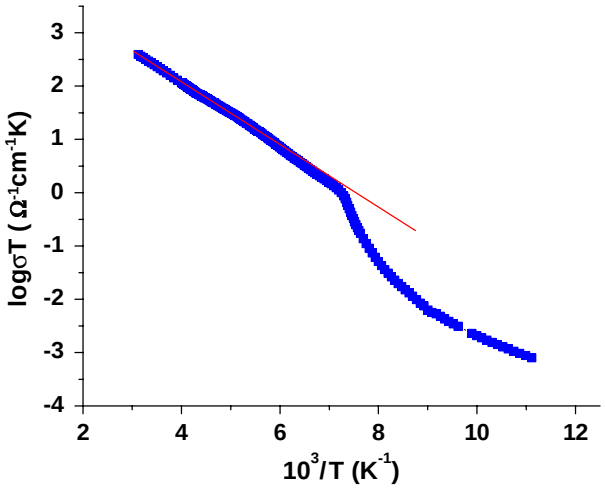

Fig. 8. Fit of the conductivity of $BaV_{10}O_{15}$, $T_s = 135$ K, to the Mott Polaronic Model. The derived activation energy is 0.120(1) eV.

3.5. Samples with $T_s = 135$ K

There is a clear and dramatic break at $T = 136(1)$ K, essentially T_s. For $T > T_s$ the data can be fit, roughly, to a simple Arrhenius law, whereas, this simple approach clearly fails for $T < T_s$. Taking the $T > T_s$ data first, a number of possible transport models have been proposed for narrow band materials, such as transition metal oxides, which are consistent with Arrhenius-like behavior and involve versions of activated processes falling under the heading of small polaronic conduction [38]. In most models an equation such as (1) below is used

$$\sigma = AT^{-n}[\exp(-W/kT)], \quad (1)$$

where σ is the conductivity, W the activation energy for electron hopping, $A = [c(1-c)e^2 v_0/kR]$ where c is the concentration of lower-valent polaron states, v_0 is the characteristic hopping frequency, R is the average hop distance and $n = 1$ if the hop occurs adiabatically. For non-adiabatic hopping, considered to be less likely [39], $n = \frac{3}{2}$. In Fig. 8 the data are fitted according to (1) with $n = 1$ and it is noted that this is superior to the simple Arrhenius approach ($n = 0$ in the prefactor) as the linearity range is extended down to 136 from 180 K. [Results of the fit to the Arrhenius expression gives $E_a = 0.096(1)$ eV.] Constants derived from the fitting process are $W = 0.120(1)$ eV and $A = 10.32(1)\,\Omega^{-1}\,\mathrm{cm}^{-1}\,\mathrm{K}$. As a consistency check one can solve for v_0 from the A value assuming $c = 0.2$ (the V^{2+} concentration) and $R = 2.87$ Å (average V–V distance), which yields $v_0 = 2.93(3) \times 10^{12}\,\mathrm{s}^{-1}$. This is in the lower range of optical phonon frequencies, which places this material near the borderline between adiabatic and non-adiabatic hopping. Attempts to analyze the data for $T < T_s$ for these samples was much less successful. One might expect a gradual transition to

a variable-range hopping (VRH) mechanism as the temperature is lowered. Unfortunately, our data extend only to 90 K due to the large resistance of the sample below this temperature. Attempts to analyze the available data using the Hill-Zabrodskii approach to be described in the next section, where the quantity $\log dE$ vs. $\log T$ is plotted (dE is the gradient of an Arrhenius plot), did not yield a linear region. It must be concluded that the VRH regime, if present at all, occurs at lower temperatures. Nonetheless, the sharp decrease in the conductivity just below T_s is consistent with a corresponding decrease in the carrier concentration that is qualitatively compatible with V–V bond formation, which would constitute a carrier trapping mechanism.

3.6. Samples with $T_s = 105\,K$

In this case there is no clear anomaly near $T = 105$ K. This is not unreasonable as the magnitude of the susceptibility jump is much less for this sample which may imply a lesser degree of V–V bond formation and correspondingly weaker carrier trapping for this sample. Unfortunately, it was not possible to obtain single crystals of this sample which precluded a detailed study of the variation of V–V distances with temperature. The high temperature data (180–290 K) were fitted either to a simple Arrhenius law or to Eq. (1), the Mott polaronic model, yielding $E_a = 0.089(1)$ eV and $W = 0.108(1)$ eV, respectively. These values are very similar to each other and to the values found for the $T_s = 135$ K sample (0.120 eV), suggesting that there is little difference in the conduction mechanism in this thermal regime between samples at the extreme ranges of composition. Due to the relatively higher conductivity of this sample, it was possible to extend the measurements to 35 K and to search for evidence of VRH. For purposes of this analysis the conductivity can be expressed in a general form by the following equation:

$$\sigma = \sigma_0 \exp(-T_0/T)^{-n}. \quad (2)$$

Two models for VRH in three-dimensional systems are known, the original Mott model which predicts a $T^{-1/4}$ temperature dependence, and the Efros-Shklovskii (ES) model which includes the effects of electron correlation resulting in a $T^{-1/2}$ law [40,41]. It is notoriously difficult to distinguish between these power laws with conventional data analysis and, indeed, fits of the low temperature data to either the Mott or ES models for this sample appeared to be of equal quality. Hill and Zabrodskii, independently, have suggested a more rigorous test which involves the extraction of an effective activation energy, dE, from the data as below [42]

$$dE = -1/T\, d(\ln \sigma)/d(1/T) \quad (3)$$

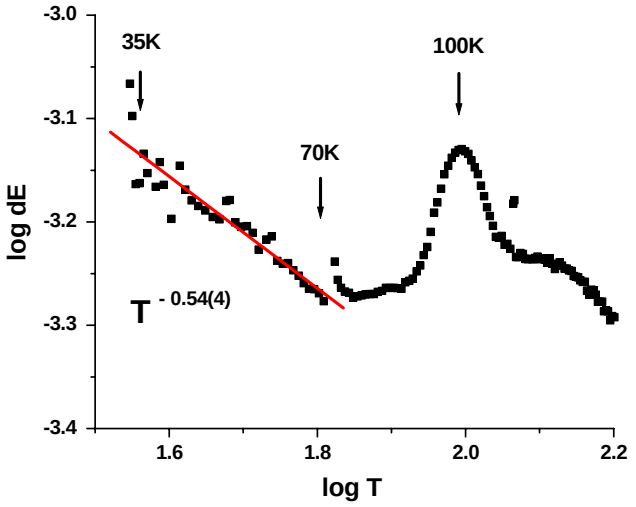

Fig. 9. Analysis of the low temperature conductivity data for $BaV_{10}O_{15}$, $T_s = 105$ K using the Hill-Zabrodskii method [41]. Agreement with the ES [40] model, $T^{-1/2}$, is clear.

and analysis by plotting $\log(\Delta E)$ vs. $\log(T)$ which allows extraction of the exponent from the slope of any linear region according to

$$\log dE = A + n \log T. \quad (4)$$

Data from 65 to 35 K, analyzed according to Eq. (4), are shown in Fig. 9. A linear regime is found giving a slope, $n = -0.54(4)$. This seems to be evidence for the ES model which implies a correlation or Coulomb gap at the Fermi level for $BaV_{10}O_{15}$.

The temperature range for which ES behavior is observed is similar to other materials reported by Hill and Zabrodskii, which consisted of amorphous semiconductors. ES behavior has also been found up to 30 K in other correlated oxide materials, such as $Sr_2Y_{0.5}Ca_{0.5}Co_2O_7$ [43]. The characteristic temperature from $T_0 = T_{ES}$ in (2) is 2×10^3 K. This is a somewhat higher value than normally seen; for example, T_{ES} for $Sr_2Y_{0.5}Ca_{0.5}Co_2O_7$ is 3×10^2 K. Nonetheless, the $T^{-1/2}$ law is clearly observed and there are few other tenable explanations. Note, finally, that in the Hill-Zabrodskii plot a prominent anomaly is seen near 105 K, the T_s value for this sample, which was not evident in a standard Arrhenius plot.

3.7. Thermopower data for $T_s = 105\,K$ and 135 K samples

Thermopower data on these samples are shown in Fig. 10a. Two facts are immediately obvious. First, the thermopower is positive over the entire temperature range, indicating that holes are the predominant carriers in $BaV_{10}O_{15}$. Secondly, the data show a very strong temperature dependence with near zero values down to 250 K, which increase rapidly as the temperature is lowered further. Careful examination indicates an

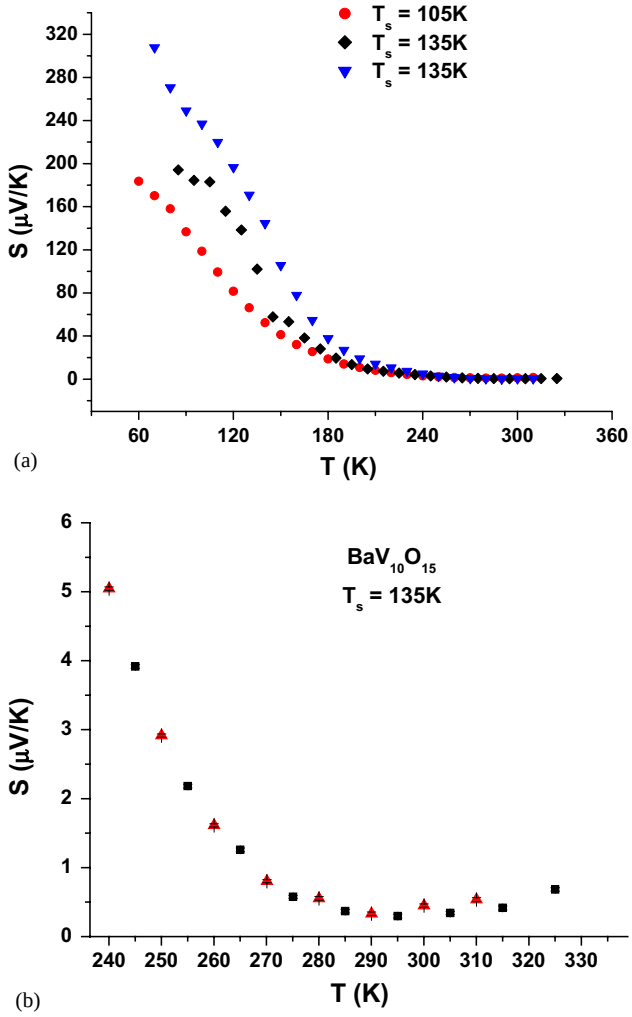

Fig. 10. (a) (TOP) Temperature dependence of the Seebeck coefficient for $BaV_{10}O_{15}$ samples with $T_s = 105$ and 135 K. (b) (BOTTOM) Thermopower for $BaV_{10}O_{15}$ with $T_s = 135$ K near room temperature. The different symbols represent different runs for the same sample.

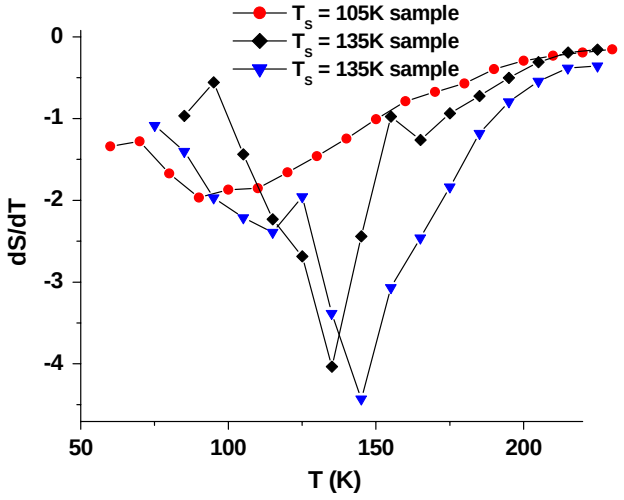

Fig. 11. Temperature derivative of the Seebeck coefficient for the samples in Fig. 10a.

inflection point near T_s, seen most clearly in the plots of dS/dT for the 135 K samples, Fig. 11. Though the anomaly is less well defined for the 105 K material, its presence in both samples is further evidence for a dramatic decrease in carrier concentration below T_s.

A quantitative understanding is more difficult to realize. The conductivity data seem to support a small polaron or electron hopping model for the high temperature regime, at least. On this basis one would expect a very different set of thermopower data. First, the simplest small polaron model involves the Heikes formula given below [44]:

$$S = -(k/e)\ln[(1-p)/p], \quad (5)$$

where p is the ratio of carriers to available sites. Taking $p = [V^{2+}] = 0.2$, the expected $S = -119\,\mu V/K$ which is temperature independent. While the Seebeck coefficient is constant over the range ~ 270–~ 330 K the values range from $+0.4$ to $+1.2\,\mu V/K$ for samples with T_s values from 135 to 105 K, respectively, as seen from Fig. 11. As the thermopower increases to the range 200–300 μV/K at 50 K, this simple approach is clearly wrong. On the Heikes model or in fact any more sophisticated approach that takes electron or spin correlation into account [45] a value of $p \cong 0.5$ would be needed. This suggests a two carrier model with both holes and electrons with details such that at higher temperatures the two contributions are nearly equivalent while at lower temperatures the holes dominate. That is, the phase transition must somehow trap electrons, predominantly.

At this stage it seems that comparison with Cr-doped V_2O_3 would be useful. As already emphasized, $BaV_{10}O_{15}$ may be regarded as a heavily doped version of V_2O_3, which is in fact equivalent, electronically, to 20% Cr^{3+}, i.e., $Cr_{0.4}V_{1.6}O_3$. Unfortunately, the maximum doping range which has been well studied for V_2O_3 extends at most to $\sim 6\%$ Cr. Nonetheless, the available, albeit scant, results for high Cr doping levels indicate positive room temperature Seebeck coefficients of a few μV/K which rise rapidly as the temperature decreases [46], i.e., parallel to the behavior of $BaV_{10}O_{15}$ although there is no phase transition in Cr-doped V_2O_3.

A possible model for the electronic structure of $BaV_{10}O_{15}$ involves as a starting point something analogous to Cr-doped V_2O_3, i.e., an electron doped Mott-Hubbard insulator. The high electron doping levels (20% V^{2+}–d^3) would introduce a significant aperiodic perturbation, i.e., Anderson localization, and significant mobility edges to the bands. The Fermi level would be placed such as to mimic the situation for an intrinsic semiconductor and roughly equivalent densities of states for holes and electrons. As the temperature is lowered through the phase transition,

states from the nominal conduction band are removed due to V–V bond formation and electronic carriers are removed permitting hole conduction to predominate at low temperatures.

3.8. Summary and conclusions

$BaV_{10}O_{15}$ is a highly correlated, mixed-valence (V^{2+}/V^{3+}) vanadium oxide with a crystal structure and composition very similar to that of the well-studied V_2O_3. It exhibits a remarkable crystallographic phase transition below T_s. T_s varies from 135 to 105 K as the sample becomes more oxidized, i.e., as the V^{2+} content is diminished. DSC studies indicate that the transition is largely first-order showing a latent heat and hysteresis with a value for $\Delta S_{trans} \sim R \ln 2$ which is consistent with a two configuration problem. Evidence from X-ray and neutron diffraction shows a change in space group symmetry from *Cmca* above T_s to *Pbca* below T_s and discontinuous changes in cell constants. There is no convincing evidence for charge ordering from the crystallographic data. Examination of V–V distances in the high and low temperature forms discloses that for one pair of V atoms involved in an intercluster link, a 7% decrease in interatomic distance occurs suggesting partial bond formation as the driving force for the transition. Thus, while the crystal structure of $BaV_{10}O_{15}$ is more related to V_2O_3 the origin of the phase transition more closely resembles that in rutile structure VO_2 and the related Magneli phases, V_4O_7 and V_5O_9. Transport property measurements show that all samples of the compound are semiconducting at all temperatures studied. The $T_s = 135$ K sample shows a pronounced decrease in conductivity below the phase transition, while this effect is more subtle for the $T_s = 105$ K material. Analysis of the high temperature conductivity data for both samples suggests a polaronic hopping model, and thermopower data require a quite complex situation. The room temperature Seebeck coefficient is anomalously small and positive, $S \sim +1\,\mu V/K$, and increases sharply with decreasing temperature to values near $+200\,\mu V/K$ with a clear anomaly at T_s. This observation is consistent with a two carrier model with essentially equal densities of states and mobilities for holes and electrons at high temperatures but for which electron states are removed due to V–V bond formation below T_s. It is worth noting that the related V^{2+}/V^{3+} vanadium oxides, $BaV_{13}O_{18}$ and $SrV_{13}O_{18}$, show n-type conductivity over the same temperature range, indicating a profound difference in electronic structure [25]. Finally, analysis of the low temperature conductivity data for the $T_s = 105$ K sample of $BaV_{10}O_{15}$ using the Hill–Zabrodskii method shows clear evidence for correlated, Efros-Shklovskii, variable-range hopping at low temperatures, strong evidence for the importance of correlation in this partially disordered, transition metal oxide.

Acknowledgments

We thank Professors R.W. Datars, J. Britten, and M.A. White for helpful discussions. C.A.B. was supported by an OSSTF award from the government of Ontario and J.E.G. by the Natural Sciences and Engineering Research Council of Canada through a Research Grant. We thank the following for assistance with various procedures and the collection of data: J.D. Garrett and H.F. Gibbs of the Brockhouse Institute for Materials Research, high temperature synthesis and thermal analysis, respectively; Ian Swainson of the Neutron Program for Materials Research of the NRC, the neutron diffraction experiments; Pamela Collins, ICPMS data; and J.F. Britten, single crystal X-ray diffraction.

References

[1] M. Foëx, C. R. Acad. Sci. 223 (1946) 1126;
F.J. Morin, Phys. Rev. Lett. 3 (1959) 34.
[2] P.D. Dernier, M. Marezio, Phys. Rev. B 2 (1970) 3771.
[3] R.M. Moon, Phys. Rev. Lett. 8 (1970) 527.
[4] W.F. Brinkman, T.M. Rice, Phys. Rev. B 2 (1970) 4302.
[5] J.B. Goodenough, Prog. Solid State Chem. 5 (1972) 145.
[6] J. Spalek, A. Datta, J.M. Honig, Phys. Rev. Lett. 59 (1987) 728.
[7] J.-H. Park, L.J. Tjeng, A. Tanaka, J.W. Allen, C.T. Chen, P. Metcalf, J.M. Honig, F.M.F. de Groot, G.A. Sawatzky, Phys. Rev. B 61 (2000) 11506.
[8] D.B. McWhan, T.M. Rice, J.P. Remeika, Phys. Rev. Lett. 23 (1969) 1384.
[9] H. Kuwamoto, J.M. Honig, J. Appel, Phys. Rev. B 22 (1980) 2626.
[10] H. Seo, H. Fukuyama, J. Phys. Soc. Japan 67 (1998) 2602;
T. Ohama, H. Yasuoka, M. Isobe, Y. Ueda, Phys. Rev. B 59 (1999) 3299;
M.V. Mostovoy, D.I. Khomskii, Solid State Commun. 113 (1999) 159.
[11] M. Marezio, P.D. Dernier, D.B. McWhan, S. Kachi, J. Solid State Chem. 11 (1974) 301.
[12] J.-L. Hodeau, M. Marezio, J. Solid State Chem. 23 (1978) 253.
[13] Y. Kanke, K. Kato, E. Takayama-Muromachi, Y. Matsui, J. Solid State Chem. 89 (1990) 130.
[14] Y. Kanke, Phys. Rev. B 60 (1999) 3764.
[15] Y. Hata, Y. Kanke, E. Kita, H. Suzuki, G. Kido, J. Appl. Phys. 85 (1999) 4768.
[16] O. Mentre, Y. Kanke, A.-C. Dhausy, P. Conflant, Y. Hata, E. Kita, Phys. Rev. B 64 (2001) 174404/1-11
[17] Y. Kanke, E. Takayama-Muromachi, K. Kato, K. Kosuda, J. Solid State Chem. 113 (1994) 125.
[18] Y. Kanke, E. Takayama-Muromachi, K. Kato, K. Kosuda, J. Solid State Chem. 115 (1995) 88.
[19] Y. Kanke, F. Izumi, Y. Morii, E. Akiba, S. Funahashi, K. Kato, M. Isobe, E. Takayama-Muromachi, Y. Uchida, J. Solid State Chem. 112 (1994) 429.
[20] A. Akiba, H. Yamada, R. Matsuo, Y. Kanke, T. Haeiwa, E. Kita, J. Phys. Soc. Japan 67 (1998) 1303.
[21] Y. Uchida, Y. Kanke, E. Takayama-Muromachi, K. Kato, J. Phys. Soc. Japan 60 (1991) 2530.
[22] Y. Uchida, Y. Onoda, Y. Kanke, J. Magnetism, Magn. Mater. 226–230 (2001) 446.
[23] K. Matsuno, T. Katsufuji, S. Mori, Y. Moritomo, A. Machida, E. Nishibori, M. Takata, M. Sakata, N. Yamamoto, H. Takagi, J. Phys. Soc. Japan 70 (2001) 1456.

[24] K. Iwasaki, H. Takizawa, K. Uheda, T. Endo, M. Shimada, J. Solid State Chem. 158 (2001) 61.
[25] K. Iwasaki, H. Takizawa, H. Yamame, S. Kubota, J. Takahashi, K. Uheda, T. Endo, Mater. Res. Bull. 38 (2003) 141.
[26] D. Chales de Beaulieu, H. Muller-Buschbaum, Z. Anorg. Allgem. Chem. 472 (1981) 33.
[27] G. Liu, J.E. Greedan, J. Solid State Chem. 122 (1996) 416.
[28] R.D. Shannon, Acta. Crystallogr. A 32 (1976) 751.
[29] SAINT release 4.05. Siemens Energy and Automation Inc. Madison WI, 1996.
[30] G.M. Sheldrick, SADABS: Siemens Area Detector Absorption Correction Software, University of Göttingen, Germany, 1996.
[31] G.M. Sheldrick, SHELXL97, Program for the Refinement of Crystal Structures, University of Göttingen, Germany, 1997.
[32] G. Amow, N.P. Raju, J.E. Greedan, J. Solid State Chem. 155 (2000) 177.
[33] I.D. Brown, D. Altermatt, Acta. Crystallogr. B 41 (1985) 244.
[34] A.S. Wills, VaLIst for GSAS, 1998.
[35] G. Andersson, Acta. Chem. Scand. 10 (1956) 623.
[36] D.B. McWhan, J.P. Remeika, M. Marezio, P.D. Dernier, Phys. Rev. B 10 (1974) 490.
[37] G.V. Chandrashekhar, H.L.C. Barros, J.M. Honig, Mater. Res. Bull. 8 (1973) 369.
[38] T. Holstein, Ann. Phys. 8 (1959) 343;
A. Ghosh, J. Chem. Phys. 102 (1994) 1385.
[39] D. Emin, Phys. Rev. B 48 (1993) 13691.
[40] N.F. Mott, Conduction in Non-Crystalline Materials, Oxford University Press, New York, 1987, pp. 20–29.
[41] A.L. Efros, B.I. Shklovskii, J. Phys. C: Solid State Phys. 8 (1975) L49.
[42] R.M. Hill, Phys. Stat. Sol. A 35 (1976) K29;
A.G. Zabrodski, Sov. Phys. Semicond. 11 (1977) 345.
[43] K. Yamaura, D.P. Young, R.J. Cava, Phys. Rev. B 63 (2001) 64401.
[44] R.R. Heikes, J.R.W. Ure, thermoelectricity: science and engineering, in: p.M. Chaikin (Ed.), An Introduction to Thermopower for those who Might want to use it to Study Organic Conductors and Superconductors, Organic Superconductivity, Interscience Publishers, New York, 1961;
V.Z. Kresin, W.A. Little Plenum Press, New York, 1990.
[45] P.M. Chaikin, P. Beni, Phys. Rev. B 13 (1976) 647.
[46] A.P.B. Sinha, G.V. Chandrashekhar, J.M. Honig, J. Solid State Chem. 12 (1975) 402.